


# Integral field unit for the existing imaging and spectroscopy instrument, FOCAS

Shinobu OZAKI <sup>1,\*</sup> Mitsuhiro FUKUSHIMA,<sup>1</sup> Hikaru IWASHITA,<sup>1</sup> Kenji MITSUI,<sup>1</sup> Takashi HATTORI,<sup>2</sup> Chien-Hsiu LEE,<sup>2,†</sup> Yoko TANAKA,<sup>2</sup> Toshihiro TSUZUKI,<sup>1</sup> Satoshi MIYAZAKI,<sup>1</sup> Takuya YAMASHITA,<sup>1</sup> Norio OKADA,<sup>1</sup> and Yoshiyuki OBUCHI<sup>1</sup>

<sup>1</sup>National Astronomical Observatory of Japan, 2-21-1 Osawa, Mitaka, Tokyo 181-8588, Japan

<sup>2</sup>Subaru telescope, National Astronomical Observatory of Japan, 650 North A'ohoku Pl., Hilo, Hawaii 96720, USA

\*E-mail: [shinobu.ozaki@nao.ac.jp](mailto:shinobu.ozaki@nao.ac.jp)

†Present address: NSF National Optical-Infrared Astronomy Research Laboratory, 950 N. Cherry Ave., Tucson, AZ 85719, USA.

Received 2020 April 8; Accepted 2020 September 3

## Abstract

The Faint Object Camera and Spectrograph (FOCAS) is an optical imaging and spectroscopy instrument for the Subaru Telescope. It has been a workhorse instrument since the first-light phase of the telescope. We describe an integral field unit (IFU) that has recently been installed in FOCAS. The IFU utilizes an image slicer that divides a  $13''.5 \times 10''.0$  field of view into 23 stripes, with a width of  $0''.435$ . A sky spectrum separated from an object by approximately  $5''.2$  can be obtained at the same time as an object spectrum. Test observations confirmed that the image quality of the IFU does not degrade the  $0''.435$  sampling, and that slice width and length are consistent with the design. Highly reflective multilayer dielectric coatings were coated on all the mirrors in the IFU, thereby offering a high mean IFU throughput of  $\sim 85\%$  over the field. However, the outer part of the field showed throughput degradation, which was mainly caused by vignetting as a result of misalignment. The flat-fielding accuracy was degraded by the vignetting, with the variation depending on the direction of the telescope.

**Key words:** instrumentation: spectrographs — techniques: imaging spectroscopy — techniques: spectroscopic

## 1 Introduction

Integral field spectroscopy (IFS) enables researchers to obtain data with three dimensions (two spatial and one wavelength) in one exposure. This method provides a homogeneous data set that is not affected by observation conditions and is suitable for a detailed study of extended objects such as galaxies. In addition, telescope time can be used more efficiently than with scanning methods such as slit scan. This capability is important, especially for

large telescopes with expensive telescope runtimes. Because of these advantages, IFS is becoming a major technique in optical and infrared observations, and many telescopes currently have integral field spectrographs (e.g., Allington-Smith et al. 2002; Larkin et al. 2003; McGregor et al. 2003; Bacon et al. 2010; Sharples et al. 2014; Morrissey et al. 2018).

At the Subaru Telescope, an integral field spectrograph named Kyoto 3DII (Sugai et al. 2010) was commissioned.

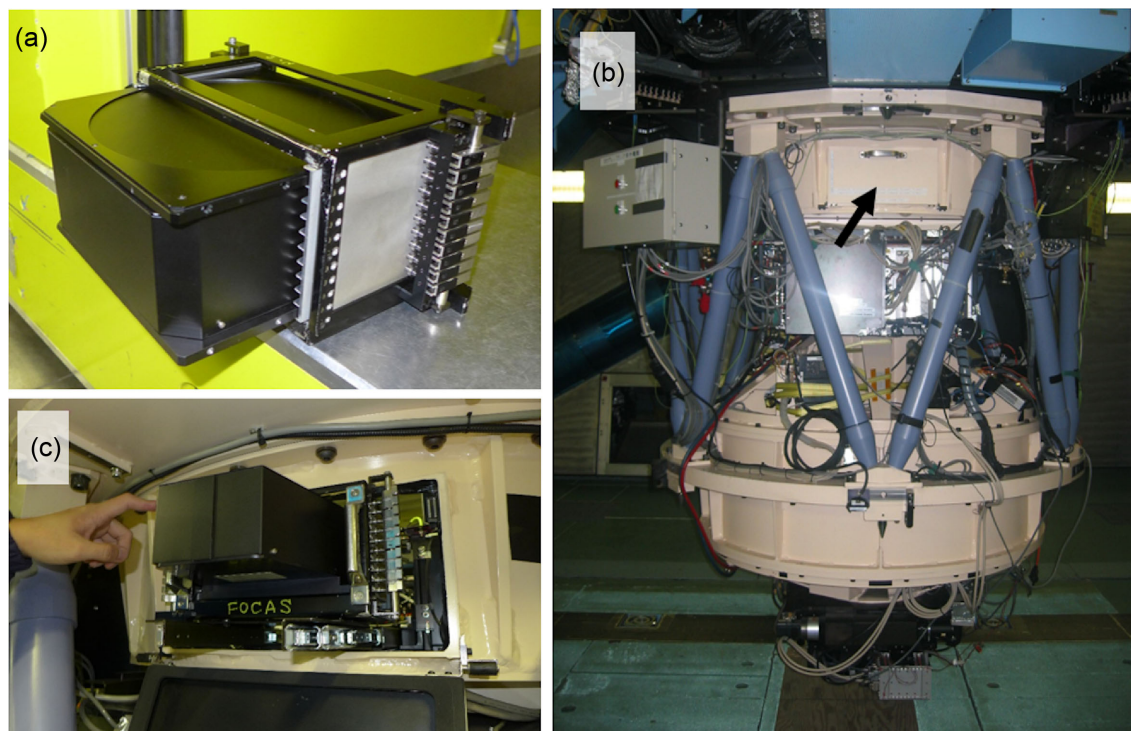


**Fig. 1.** (a) FOCAS mask storage containing the IFU and one mask plate. (b) Installation of the mask storage to FOCAS. (c) Entire view of FOCAS. The black arrow shows the hatch for the mask storage installation seen in panel (b). (Color online)

Its spatial sampling was originally optimized for a 2 m telescope and was very fine ( $0''.096$ ). This fine sampling provided a unique capability of adaptive-optics-assisted optical IFS (Kawaguchi et al. 2018; Matsubayashi et al. 2016). However, due to the fine sampling and its low efficiency ( $\sim 2\%–10\%$ ), the detection limit was shallow for extended objects. Therefore, we were motivated to develop a high-throughput integral field unit (IFU) optimized for the Subaru Telescope in order to observe faint extended objects.

The IFU is designed to be installed into an existing instrument, the Faint Object Camera And Spectrograph (FOCAS; Kashikawa et al. 2000, 2002). FOCAS is an optical imaging and spectroscopy instrument mounted on a Cassegrain focus of the Subaru Telescope and has been a workhorse instrument since the telescope began operation. Using an existing instrument, development time and cost can be reduced, which is very important in today's extremely large telescope era.

The development of FOCAS IFU began in 2010 and was completed in 2017. Our initial development work, including prototyping, was reported in our previous papers (Ozaki et al. 2012, 2014). After a commissioning run in 2018 March, the IFU was accepted for common use in 2018 July and has been operational since the first semester of 2019. The first scientific paper has already been published (Smith et al. 2020).

In the present paper, our concept is briefly introduced in section 2. The optical layout and the mechanical structure of FOCAS IFU are explained in sections 3 and 4. In section 5, the reduction software developed for FOCAS IFU is described. Then, the performance verified in the commissioning runs is reported in section 6.

## 2 Concept

FOCAS originally offered slit spectroscopy and imaging functions. We wanted the IFU mode to accommodate with these functions without any refurbishment of FOCAS. Therefore we decided to store the IFU in an existing slit mask storage and use an existing mask exchange mechanism for deploying the IFU to the light path. The storage has 10 mask slots (figure 1a). The IFU occupies nine slots, and one slit mask can be installed along with the IFU. This one additional slit mask allows for flexible operation. The storage is installed to FOCAS in the usual manner (figures 1b and 1c). After the mask exchange mechanism extracts the IFU from the storage and puts it on the focal plane stage, the IFU is fixed with the existing three air cylinders also used for fixing a mask plate (figure 2). These air cylinders have sufficient force to hold the IFU. Although this concept required no refurbishment of FOCAS itself, it caused tight space and weight constraints on the IFU.

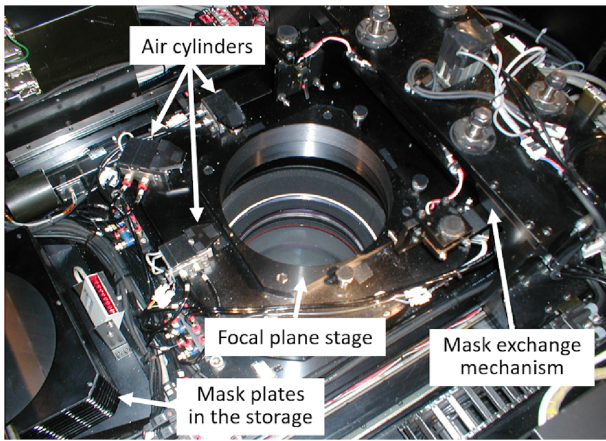


**Fig. 2.** Inside view around the telescope focal plane in FOCAS. At the left of this picture, 10 mask plates in the storage can be seen. Three air cylinders for fixing the mask plate and the IFU are located around the focal plane stage. The mask exchange mechanism is at the right. (Color online)

### 3 Optical layout

There are three main methods for IFS: a lenslet array system such as Kyoto 3DII (Sugai et al. 2010) and OSIRIS (Larkin et al. 2003), a fiber-bundle system such as GMOS IFU (Allington-Smith et al. 2002) and VIMOS IFU (Prieto et al. 2000), or an image slicer system such as KCWI (Morrissey et al. 2018) and MUSE (Bacon et al. 2010). Among the three methods, the final system utilizes the detection area most effectively, thereby obtaining the most information. Because of this advantage, we selected the image slicer system for FOCAS IFU.

The slice width was set to approximate the best seeing size ( $\sim 0''.4$ ) to resolve object structures, and the aspect ratio of the field of view (FoV) was set to about 1.4 because most extended objects show elongation. Together with the total slit length ( $\sim 6'$ ) accepted by FOCAS, the FoV and the number of slices were derived to be  $10'' \times 13''.5$  and 23, respectively.

The optical layout of FOCAS IFU is shown in figures 3 and 4. It was based on the Advanced Image Slicer layout (Content 1997) used in GNIRS IFU (Allington-Smith et al. 2006). The basic IFU parameters and the designed optical parameters are summarized in tables 1 and 2.

Light from the telescope is reflected by a flat pick-off mirror located before the telescope focus and at the outskirts of the telescope FoV. At the telescope focus, a field stop limits the field size along the slice-length direction. The field size along the perpendicular direction is limited by the slicer. An object image is magnified 5.28 times via magnification optics consisting of a doublet lens, a small folded mirror, and a concave spherical mirror. The output beam from the magnification optics is telecentric and goes to the image slicer.

**Table 1.** FOCAS IFU parameters.

Field of view*	$13''.42 \times 10''.0$
Slice length*	$13''.42$
Slice width*	$0''.435$
Number of slices	23
Wavelength coverage	370–1000 nm
Sky slit length	$13''.5$
Sky slit width	$0''.435\text{--}0''.577^\dagger$

\*These are measured values (see subsection 6.3).

$^\dagger$ The width is gradually changed along the slit.

**Table 2.** Designed optical parameters.

Magnification optics	
Focal length of the doublet lens	45 mm
ROC* of the spherical mirror	477 mm (concave)
Magnification factor	5.28
IFU part	
ROC* of the slice mirrors	500 mm (concave)
Physical slice width	$1.111\text{ mm}^\dagger$
ROC* of the pupil mirrors	79 mm (concave) $^\ddagger$
ROC* of the slit mirrors	61 mm (concave)

\*Radius of curvature.

$^\dagger$ This value is measured with a micrometer.

$^\ddagger$ For the ellipsoidal surfaces, this is the radius of an approximate sphere.

The image slicer consists of 23 slice mirrors with a curvature radius of 500 mm. The reflection surface of each slice mirror is 1.111 mm in width and 41 mm in length. For the width, a value measured with a micrometer was adopted in the design. The image slicer slices the magnified image into 23 stripes and creates pupil images on the relevant pupil mirrors. We refer to the 23 slice channels as Ch01–Ch23.

The pupil mirrors reimage the sliced images with a magnification factor that is the inverse of the magnification optics. The pupil mirrors in the outer channels (Ch01–Ch06 and Ch18–Ch23) have off-axis ellipsoidal surfaces optimized for each channel to reduce aberrations from large reflection angles. Their approximate curvature radii are  $\sim 79$  mm, and the surfaces are a 6.5 mm square. In terms of the inner channels (Ch07–Ch17), the pupil mirrors have identical spherical surfaces with a curvature radius of 79 mm, and their surfaces are round with a diameter of 6.5 mm.

Slit mirrors are located at the pseudo slits and bring the exit pupil to infinity. The focal ratio and exit pupil location of the output light are similar to those of the telescope. All slit mirrors have an identical spherical surface with a curvature radius of 61 mm. This curvature radius was selected to minimize the vignetting caused in FOCAS. The largest vignetting is  $\sim 4\%$  at the edge of the Ch01 pseudo slit in the design. There is a gap between the pseudo slits of Ch12 and Ch13. This is to match the gap between two CCDs of FOCAS.



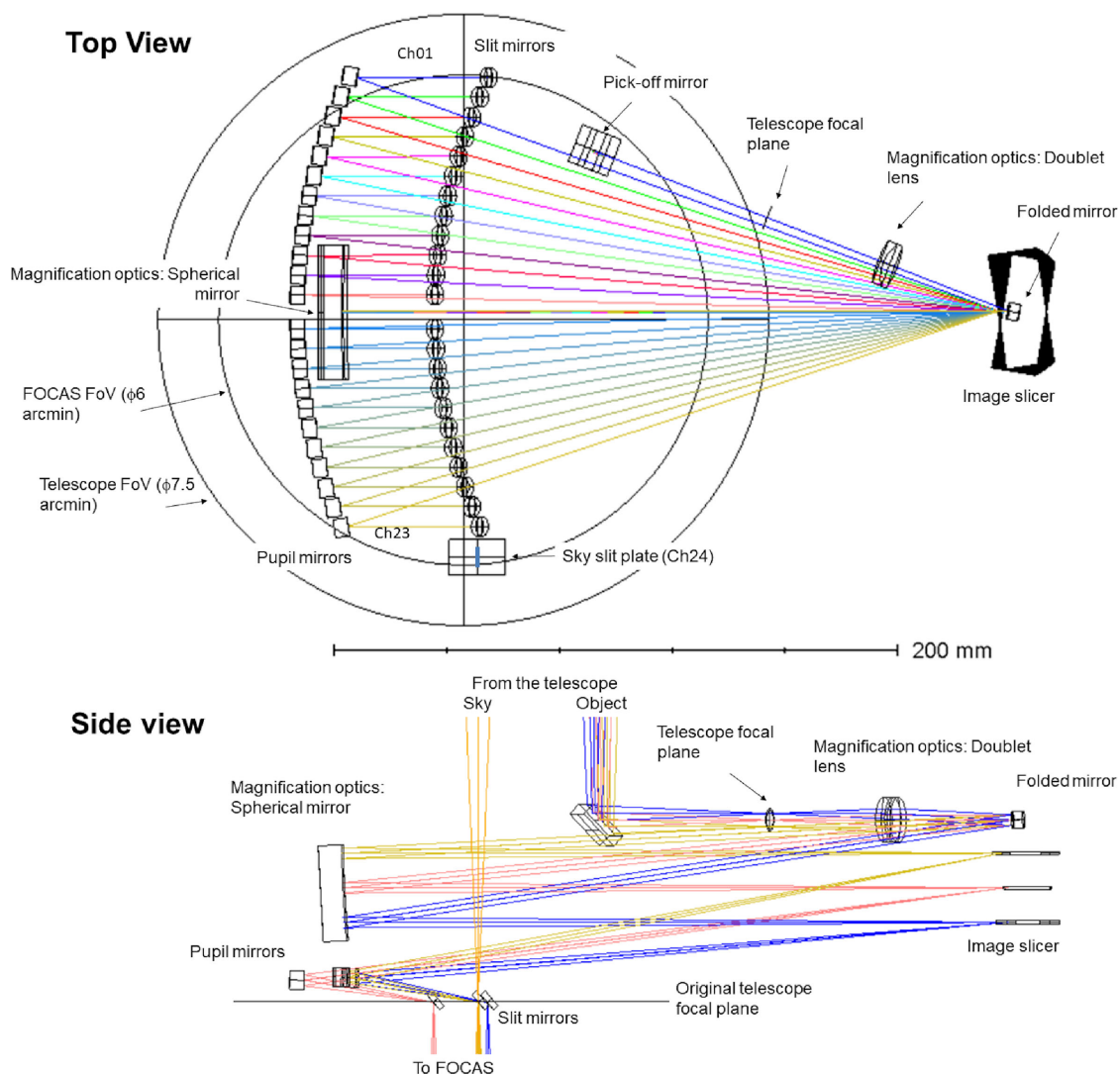


**Fig. 3.** Optical layout of FOCAS IFU. The top and bottom panels show the top and side views, respectively. In the top view, only the chief rays are shown for clarity. The two circles show the FoVs of the telescope ( $\phi 7.5$ ) and FOCAS ( $\phi 6'$ ). The object pick-up position and the sky slit are away from the telescope field center. The sky slit plate is next to the slit mirror of Ch23. The thick blue line shows the slit location in the plate. In the side view, only Ch01, Ch12, Ch23, and the sky channel (Ch24) are shown. Sky light passes through the IFU optics and goes directly to the FOCAS optics via the sky slit. The slit mirrors and the sky slit plate locate on the original telescope focal plane. (Color online)

A slit for sky light is located next to the Ch23 slit mirror and on the original telescope focal plane. We refer to the sky channel as Ch24. The slit is  $\sim 5/2$  away from the object pickup position. The sky light passes through the IFU optics and goes directly to the FOCAS optics. The slit width gradually changes along the slit, which enables us to select an optimum width in the sky subtraction process (see section 5).

Spot root-mean-square (RMS) diameters at the center and two edges of the pseudo slits are shown in figure 5, where the beneficial effect of the off-axis ellipsoidal surfaces of the pupil mirrors can be clearly observed. Ch01 and Ch07 show the worst image quality among the channels using spherical and ellipsoidal surfaces,

respectively. Spot diagrams and wavelength dependencies of the spot RMS diameters of these two channels are shown in figures 6 and 7. For almost all wavelength ranges, the RMS spot diameters are less than  $40 \mu\text{m}$ , corresponding to  $0''.275$ .

The largest fan angle of the slice mirror is  $\sim 9.95$ . The fan angle causes image blur due to off-focus. However, owing to a large input F ratio of  $\sim 64^1$  into the slicer, the geometrical diameter of the blurring effect is  $\sim 0''.02$ , which is negligible in comparison with the slice width of  $0''.435$ .

<sup>1</sup> The telescope focal ratio is 12.2 and the magnification factor of the magnification optics is 5.28.



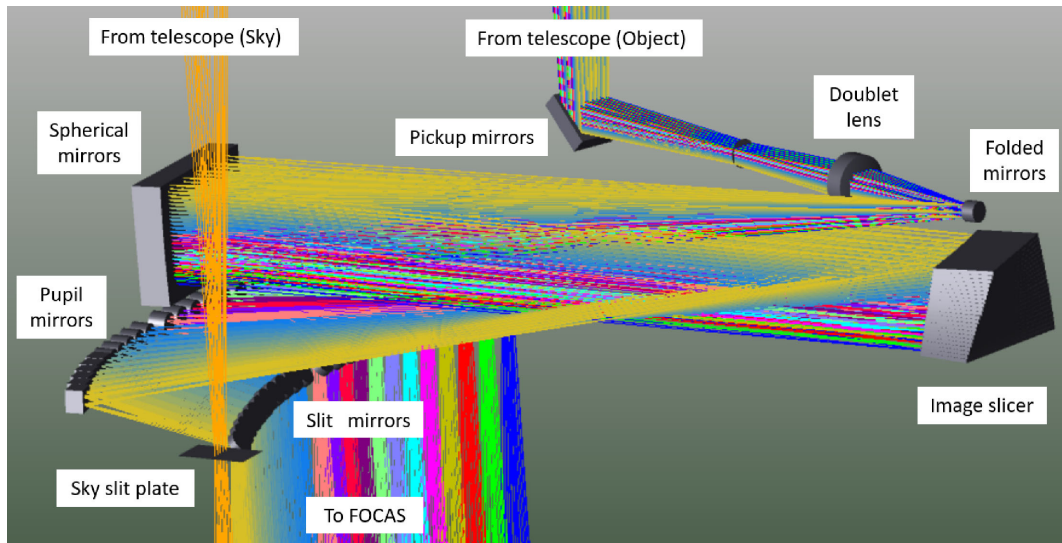


Fig. 4. Diagonal view of the shaded model. Colors show the different channels. (Color online)

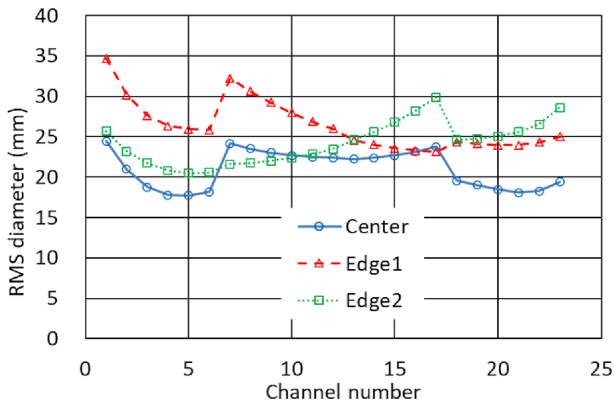


Fig. 5. Spot RMS diameters at the center and two edges of each pseudo slit. All optics from the telescope to the detector are included in this estimation. (Color online)

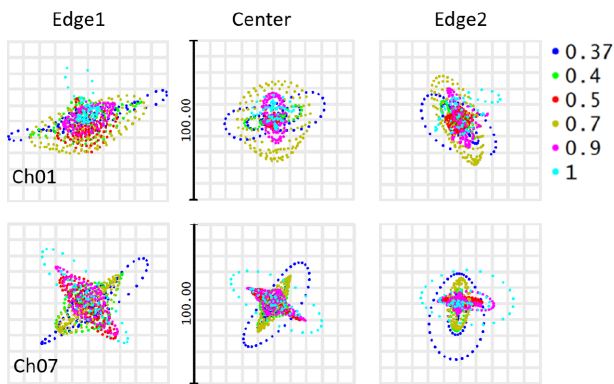


Fig. 6. Spot diagrams at the center and two edges of the pseudo slits of Ch01 and Ch07. The color coding shows wavelengths in units of  $\mu\text{m}$ . The box size in the spot diagrams is  $100 \mu\text{m}$ , corresponding to  $1''.45$ . (Color online)

#### 4 Mechanical design

The mechanical structure of FOCAS IFU is shown in figure 8. The physical dimensions are  $210 \text{ mm} \times 330 \text{ mm} \times 92 \text{ mm}$ , and the weight is 1.5 kg. The magnification optics

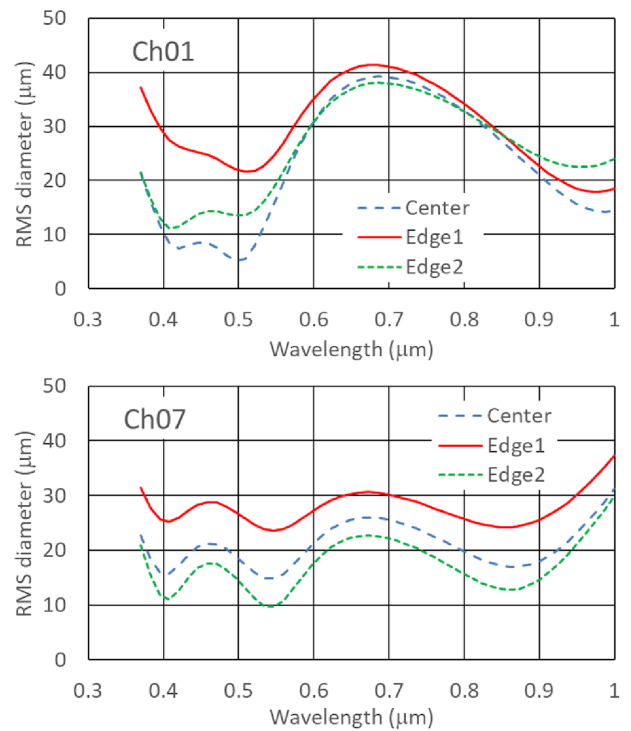


Fig. 7. Wavelength dependence of the spot radius of Ch01 and Ch07 on the detector;  $40 \mu\text{m}$  corresponds to  $0''.275$ . (Color online)

except for the spherical mirror are held in a fore-optics barrel (figure 9). The lateral position of the field stop and its rotation on the optical axis can be adjusted with fine-pitch screws.

The image slicer is shown in figure 10. The slice mirrors are placed between two thick silica plates and secured with a blade spring. We did not use glue because it was difficult to control the glue layer thickness.

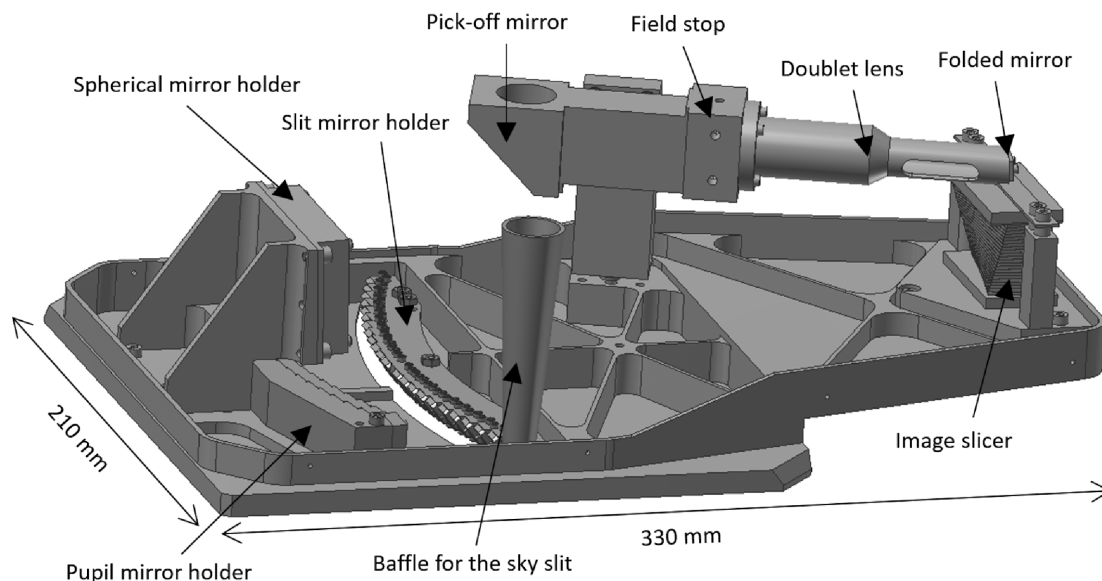


Fig. 8. Mechanical structure of FOCAS IFU.

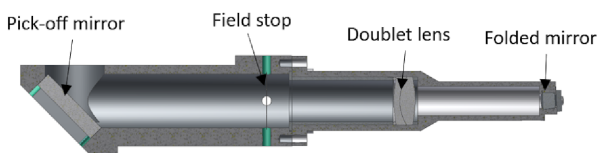


Fig. 9. Cross-section view of the fore-optics barrel, showing the pick-off mirror, field stop, doublet lens, and folded mirror.

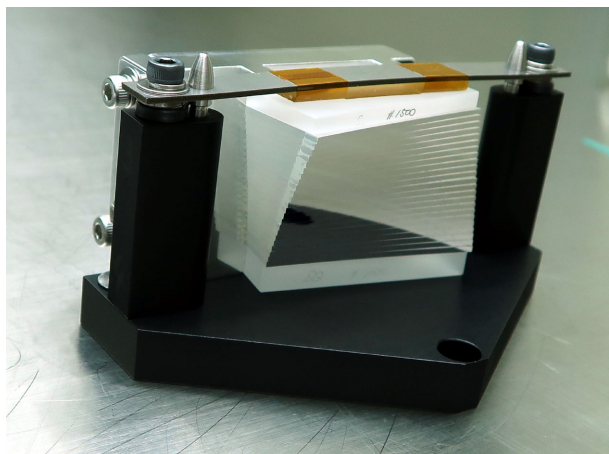


Fig. 10. Image slicer. The 23 slice mirrors were placed between the two silica plates. (Color online)

The pupil mirror array holder has 12 square holes and 11 round holes (figure 11). The square holes store the off-axis ellipsoidal surface mirrors, and the round holes store the spherical mirrors. The holder was manufactured with sufficiently high accuracy that relative alignment of each pupil mirror could be achieved without any adjustments.

The slit mirror holder holds the 23 slit mirrors with an identical shape (figure 12). When attaching the round side

of the slice mirror to a V-groove of the holder, the mirror center is located at the appropriate place (figure 13). Two black spring clips press the round side to the V-groove and the back side to the datum surface of each mirror slot.

## 5 Reduction software

The IFU data contains 23 object spectra and 1 sky spectrum (figure 14). FOCAS has two  $2K \times 4K$  CCDs, and the dispersion is in the 4K direction. Spectra of Ch01 to Ch12 are in Chip 1, and those of Ch13 to Ch24 are in Chip 2. In the IFU mode, the default readout is two-pixel binning in the spatial direction and no binning in the dispersion direction.

Reduction software was developed with Python and is distributed on the FOCAS IFU web page.<sup>2</sup> The software utilizes AstroPy<sup>3</sup> (Astropy Collaboration 2013, 2018) for FITS file handling and some fittings. In some scripts, IRAF tasks (Tody 1986, 1993) are used through the Python package PyRAF<sup>4</sup> (Science Software Branch at STScI 2012).

The bias level of the FOCAS data has a fluctuation pattern along the CCD serial register direction (the horizontal direction in figure 14). This pattern is almost stable for all images, and for all rows in one image. To remove this pattern, a template one-dimensional bias pattern is created by averaging a bias image along the vertical direction in figure 14. Then, the template is scaled with reference to relevant overscan regions for each row of other images and subtracted. After the bias subtraction, the overscan regions are removed and pixel values converted to the electron unit.

<sup>2</sup> FOCAS IFU web page (<https://www2.nao.ac.jp/~shinobuozaki/focasifu/index.html>).

<sup>3</sup> AstroPy (<https://www.astropy.org/>).

<sup>4</sup> PyRAF (<https://ui.adsabs.harvard.edu/abs/2012ascl.soft07011S/abstract>).

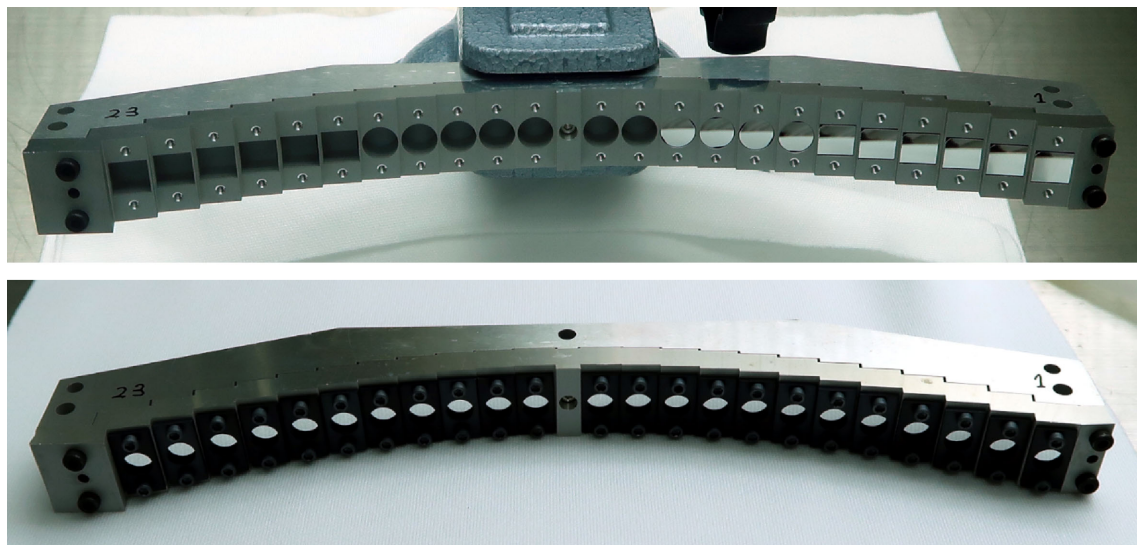


**Fig. 11.** Pupil mirror array. The upper panel shows a picture of the assembly process. The square and round holes can be clearly seen. The rightmost 10 mirrors have been installed. The bottom panel shows the finished pupil mirror array. Black retaining plates were attached for each mirror. (Color online)



**Fig. 12.** Slit mirror array. (Color online)

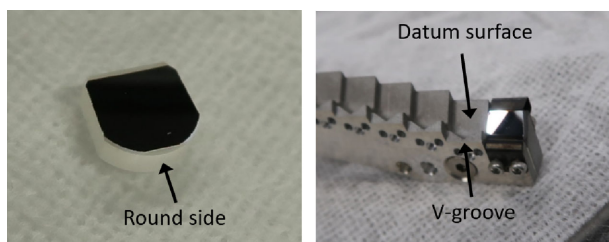


**Fig. 13.** One of the slit mirrors (left) and mirror slots of the holder (right). (Color online)

Cosmic-ray events are removed using the Python package Astro-SCRAPPY,<sup>5</sup> based on the L.A. Cosmic algorithm (van Dokkum 2001).

Prior to the flat-fielding process, the dome flat image is divided into high- and low-spatial-frequency images using a

polynomial fitting for each column. The former represents pixel-to-pixel sensitivity variation and sharp shadows of dust on the detector. The latter represents a global illumination pattern. In the flat-fielding process, the low-frequency flat image is first shifted to correct for image motion due to flexure. The image motion in the spatial direction is derived by comparing the Ch10 chip features in the dome flat image and the CAL flat image. The image motion in the dispersion direction is derived by comparing the wavelength calibration images for the dome flat and the target image. Light sources for the CAL flat and wavelength calibration are equipped in the telescope, and their data are obtained at the same telescope direction as the object. After shifting, the target image is divided by the shifted low-frequency flat image, and then by the high-frequency flat image. Figure 15 shows a demonstration of the flat-fielding. It can be seen that the Ch10 chip features are cleanly corrected.

<sup>5</sup> Astro-SCRAPPY (<https://zenodo.org/record/1482019>).



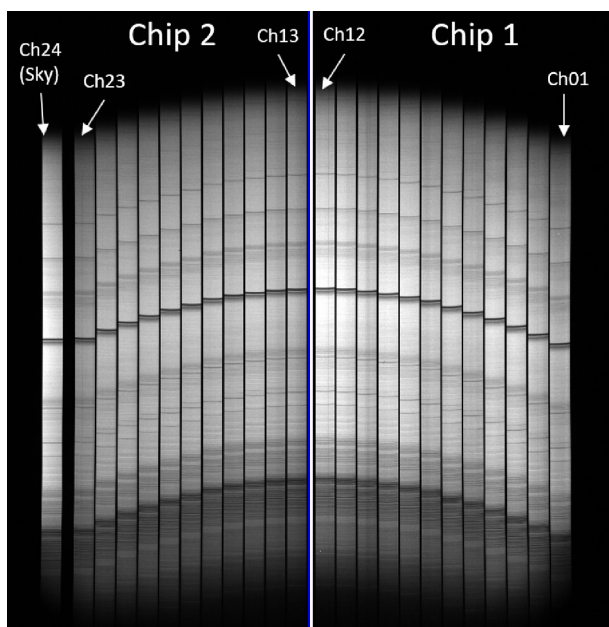


**Fig. 14.** Data example of FOCAS IFU. This is blank sky data taken with the 300R grism and the SO58 filter. The arc-like configuration of the pseudo slits can be clearly seen. The vignetting feature of the FOCAS optics can be seen at the bottom corners. At the top corners there is a similar vignetting feature, although it is not clear in this figure.

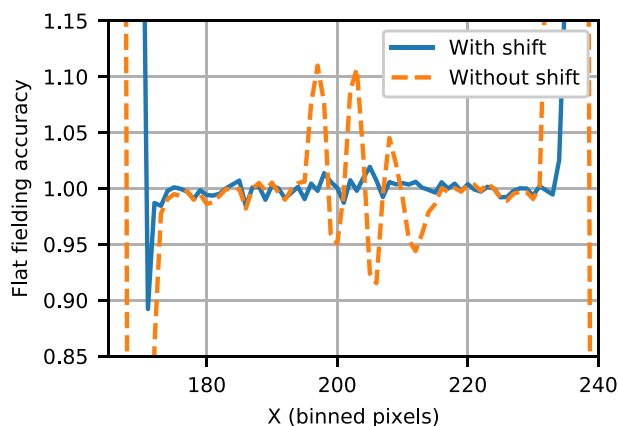


**Fig. 15.** Flat-fielding improvement using a shifted dome flat image. A normalized CAL flat image is flat-fielded by a normalized dome flat image with and without shifting. The plot shows a profile along the spatial direction at Ch10 which has some chip features around the center. Shifting the dome flat image, the flat-fielding accuracy is improved. (Color online)

After the flat-fielding, rectangular regions containing each channel spectrum are extracted and then reduced like slit-spectroscopy data. To obtain the spatial coordinate transformation functions, edge-enhanced images of the extracted CAL flat spectra are created (figure 16). Two edges of each spectrum are traced with the IRAF tasks `IDENTIFY` and `REIDENTIFY`, and the spatial coordinate transformation functions are derived using the IRAF `FITCOORDS` task. Similarly, wavelength coordinate transformation functions

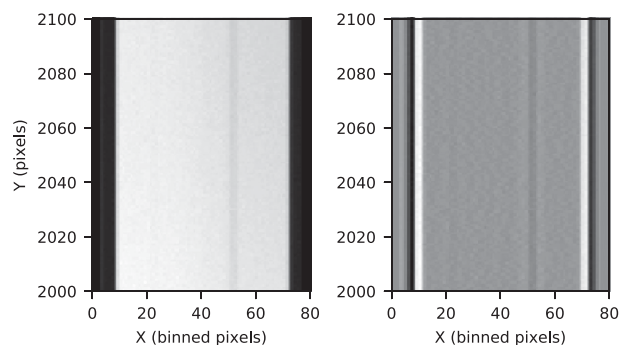


**Fig. 16.** Parts of an original (left) and an edge-enhanced (right) spectra, respectively. The dispersion is in the Y direction.

are obtained from the extracted wavelength calibration spectra using the same IRAF tasks. Together with the transformation functions, extracted spectra of an object image are transformed with the IRAF task `TRANSFORM`. A data cube is made by stacking the 24 transformed spectra.

After that, the sky background is subtracted. As previously mentioned, the sky slit width gradually changes along the slit. The measured slit width is  $0''.435$ – $0''.577$ . From trial and error, we decided that a sky spectrum was created by averaging the narrowest 10 spaxels in the slit corresponding to  $0''.435$ – $0''.455$  width. The slit width is slightly wider than the design due to a fabrication error. A more optimum slit has already been fabricated and will be replaced in the near future. Its width changes more slowly ( $0''.371$ – $0''.453$ ), and the number of spaxels for creating a sky spectrum will be increased.

In this sky subtraction method, only 10 spaxels are used. Hence, if object spectra are integrated over many spaxels (e.g.,  $>10$  spaxels), the signal-to-noise ratio is degraded. When this is critical, there are two alternate methods, although they are not implemented in the reduction software. If an object size is smaller than the IFU FoV, an outer part of the FoV can be used as the sky. Or, additional exposures for nearby blank sky can be conducted, although this consumes observation time.

Because the adopted area for the sky spectrum is at the edge of the slit, the wavelength calibration tends to have a systematic error. Although the error is at the sub-pixel level, it causes significant residuals for bright sky emission lines. To correct this error, a data cube of the wavelength calibration source is created. For the data cube, a sky-area spectrum is created in the same manner and correlated with spectra at each object-area spaxel to derive wavelength deviations. Then, the sky spectrum for the object data cube is shifted by the derived deviation and subtracted from its object spectra.

For data for a standard star, a one-dimensional spectrum is created from the data cube by integrating inside

**Table 3.** Wavelength coverage, spectral resolution, and expected sensitivity for typical dispersers.\*

Grism	Filter	Wavelength coverage <sup>†</sup> (Å)	Dispersion (Å/pixel)	$\lambda/\Delta\lambda$	Sensitivity <sup>‡</sup>		
					Wavelength <sup>§</sup> (Å)	Continuum <sup>  </sup>	Emission line <sup>#</sup>
300B	SY47	4700–7600	1.34	900	5500	2.7	1.4
300B	L600	3700–6000	1.34	900	5500	2.7	1.4
300R	SO58	5800–9550	1.34	900	7500	2.4	1.3
VPH450	L550	3870–5060	0.37	2700	4500	16	2.4
VPH520	None	4540–5830	0.39	2700	5200	8.1	1.3
VPH650	SY47	5600–7200	0.60	2300	6500	5.3	1.3
VPH850	SO58	6050–9750	1.17	1350	8200	2.4	1.1
VPH900	SO58	7850–9950	0.74	2700	9200	2.8	0.83

\*Other dispersers for FOCAS are also available in the IFU mode.

<sup>†</sup>Wavelength range covered in the whole IFU FoV.

<sup>‡</sup>The following settings are assumed: three 20 min exposures, an extended source, a dark night, two (spatial)  $\times$  one (spectral) binning, an extraction aperture of  $0''.435$  (slice width)  $\times$   $0''.43$  (two binned pixels along the slit), and a signal-to-noise ratio of 5 per spectral pixel.

<sup>§</sup>Wavelength for the sensitivity calculation.

<sup>||</sup>In units of  $10^{-18}$  erg s $^{-1}$  cm $^{-2}$  Å $^{-1}$  arcsec $^{-2}$ .

<sup>#</sup>In units of  $10^{-17}$  erg s $^{-1}$  cm $^{-2}$  arcsec $^{-2}$ . The intrinsic line width is assumed to be negligible compared to the instrument spectral resolution.

the  $5\sigma$  radius measured with the two-dimensional Gaussian fitting for the star image. The integration is performed for images at each wavelength pixel using the Photutils package.<sup>6</sup> A sensitivity function is derived using the IRAF tasks STANDARD and SENSFUNC. The sensitivity function is applied to the object spectra using the IRAF task FLUXCALIB, and atmospheric extinction is corrected using the IRAF task EXTINCTION.

## 6 Performance

The performance verification results are reported in this section. A daytime test was carried out on 2018 February 14–16, and test observations were conducted on 2018 March 2 and 2019 May 15. The weather conditions were cloudy on the former day and clear on the latter.

### 6.1 Wavelength coverage and spectral resolution

The wavelength coverage, spectral resolution, and expected sensitivity for typical dispersers are summarized in table 3. Other dispersers for FOCAS are also available in the IFU mode. The pseudo slits are located in an arc-like configuration on the detectors, and the FOCAS optics exhibits vignetting at the corners of an image (figure 14). Therefore, the wavelength coverage is different in different channels. The wavelength coverage in the table shows the ranges covered over the whole of the IFU FoV.

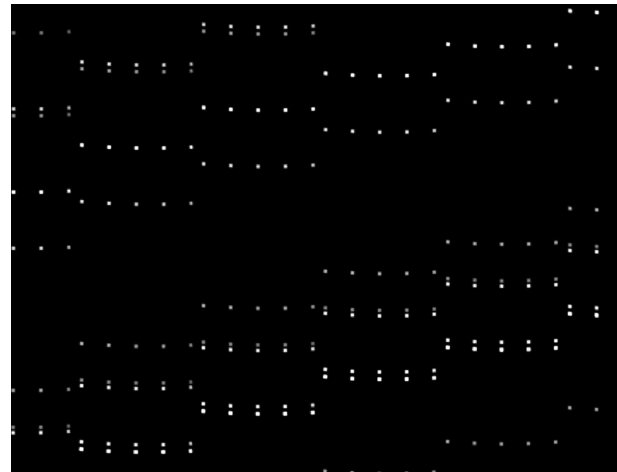


**Fig. 17.** Part of an image obtained using the test mask and the 300R grism + SO58 filter. The dispersion is in the vertical direction.

### 6.2 Image quality

For an image quality evaluation, a test mask was installed in the fore-optics barrel instead of the field stop. This mask has five slits with a width of 0.21 mm each, corresponding to  $0''.43$ . Because the slits are perpendicular to the slice-length direction, they provide a lot of boxy-shape spots when a wavelength calibration light is observed (figure 17). The evaluation data were obtained with the 300R grism and the SO58 filter in the daytime test.

Full width at half maximums (FWHMs) of the spots were measured along both spatial and dispersion directions at the peak pixels for each spot. The measured FWHMs are shown in figure 18. Both FWHMs are  $\sim 4$  pixels around the central X (X was the spatial direction), and go up to  $\sim 4.2$  pixels

<sup>6</sup> Photutils (<https://doi.org/10.5281/zenodo.596036>).

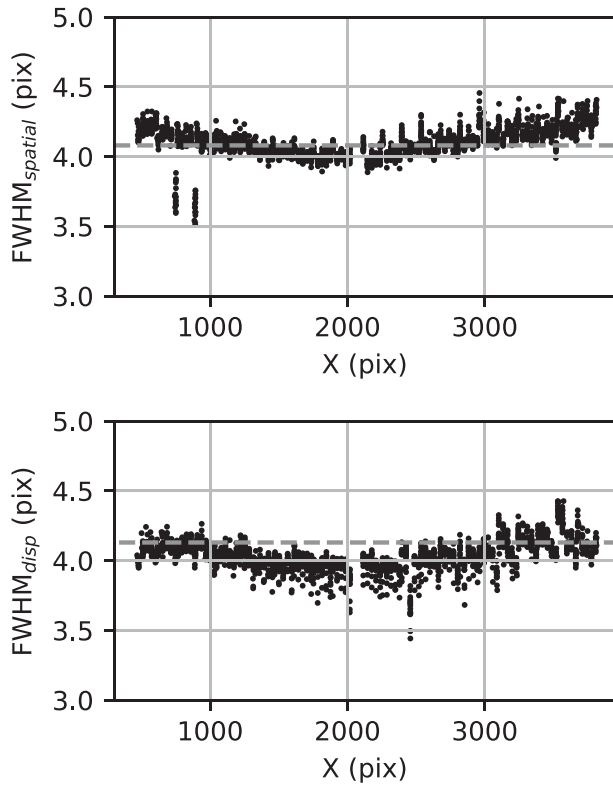


**Fig. 18.** FWHM widths along the spatial direction (upper) and along the dispersion direction (lower). The gray dashed lines in the upper and lower panels show the expected slit width of the test mask and the expected slice width, respectively.

toward the outside. This increase is explained by the distortion of the IFU and FOCAS optics. The FWHMs along both directions are almost consistent with the design. The dispersion-direction FWHMs show a slight difference from the expected results, but the difference is only  $\sim 3\%$ .

The spatial-direction FWHMs are significantly smaller at  $X \sim 750$  and  $890$ , corresponding to the rightmost spots of Ch22 and Ch21, respectively. These spots were vignetted by the relevant slice mirrors caused by a misalignment between the image slicer and the test mask (middle and bottom panels of figure 19). The dispersion-direction FWHMs are slightly smaller at  $X \sim 2460$ , corresponding to the central spots of Ch10. This is caused by chips at the edge around the Ch10 slice mirror center (upper panel of figure 19).

### 6.3 Slice width and length, and image reconstruction accuracy

To measure spatial scales, we observed an outskirts region ( $12^{\text{h}}10^{\text{m}}02^{\text{s}}.2$ ,  $+18^{\circ}32'06''.9$  J2000.0) of the globular cluster NGC 4147 on 2018 March 2 (figure 20). Six flames were obtained with an exposure time of 300 s each using the 300R grism and the SO58 filter. The seeing size measured from the stars in the image was  $\sim 0''.9$  FWHM. The obtained

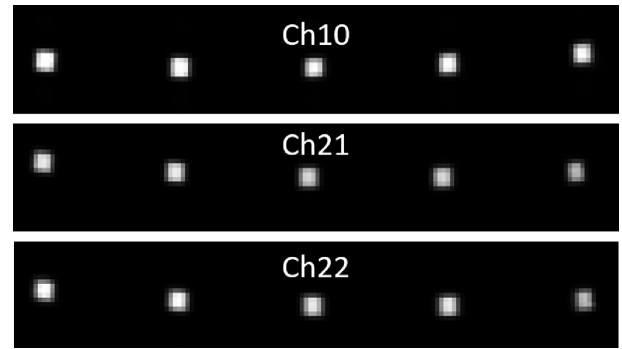


**Fig. 19.** Close-up views of Ch10, Ch21, and Ch22 in the image obtained using the test mask. The central spot of Ch10 is slightly narrower along the vertical direction than the others because of chips around the slice mirror center. The rightmost spots of Ch21 and Ch22 are narrower along the horizontal direction than the others because of the vignetting caused by the relevant slice mirrors.

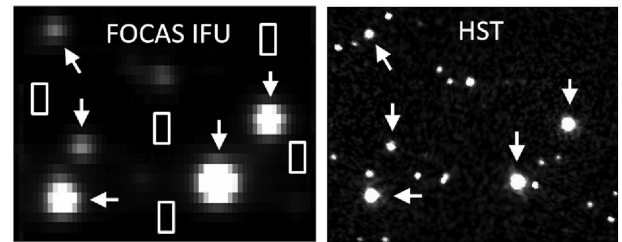


**Fig. 20.** Outskirts part ( $12^{\text{h}}10^{\text{m}}02^{\text{s}}.2$ ,  $+18^{\circ}32'06''.9$  J2000.0) of the globular cluster NGC 4147. The left panel shows an image reconstructed from the FOCAS IFU data. The right panel is the HST-V image taken from the HST Hierarchical Progressive Survey (HiPS<sup>7</sup>; Fernique et al. 2015). The stars used for the measurements are marked with arrows. The boxes show regions used for evaluating the sky subtraction accuracy (subsection 6.6). North is up and East is left.

**Table 4.** Slice width and length.

	NGC 4147	Bright star	Design
Slice width (")	$0.435 \pm 0.004$	$0.43 \pm 0.01$	0.43
Slice length (")	$13.42 \pm 0.08$	$12.9 \pm 0.4$	13.5

data were reduced with reduction software developed for FOCAS IFU, and the six sky-subtracted data cubes were all combined.

The central positions of five bright stars were derived via two-dimensional (2D) Gaussian fitting, and were compared with their celestial positions in Gaia Data Release 1 (Gaia Collaboration 2016) using the IRAF CCMAP task. The coordinate mapping uncertainty is  $\sim 0''.03$  RMS, which can be considered as the image reconstruction accuracy. The derived slice width and length are  $0''.435 \pm 0''.004$  and  $13''.42 \pm 0''.08$ , respectively, which are almost consistent with the design (table 4).

In terms of the image reconstruction accuracy, we also observed a bright spectrophotometric standard star,

<sup>7</sup> HiPS ([http://alasky.u-strasbg.fr/HST-hips/filter\\_V\\_hips/](http://alasky.u-strasbg.fr/HST-hips/filter_V_hips/)).



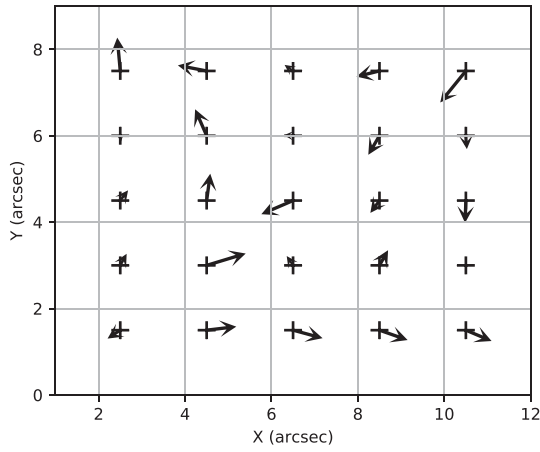


**Fig. 21.** Deviations of the measured star positions from the targeted ones (+). Arrows show the deviations magnified by 10 times.

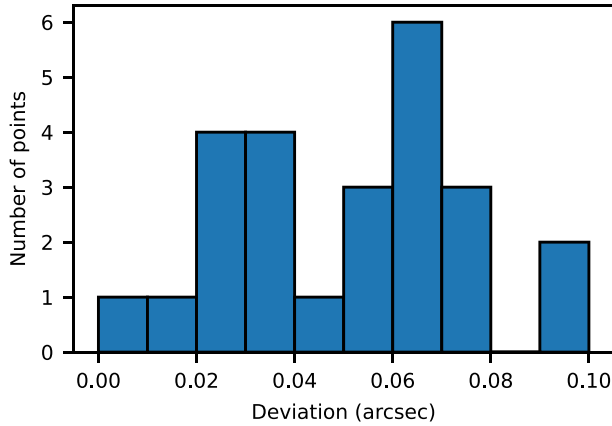


**Fig. 22.** Histogram of deviations from the targeted star positions to the measured ones.

HD 37725 ( $05^{\text{h}}41^{\text{m}}54.^{\text{s}}4$ ,  $+29^{\circ}17'51''.0$  J2000.0), using the 300R grism and the SO58 filter on 2019 May 15. The star was observed at 25 grid positions in the IFU field (figure 21) by changing guide star positions on a guiding CCD. The position steps are  $2''$  and  $1''.5$  along the RA and Dec directions, respectively. At each position, one flame with an exposure time of 10 s was obtained. The seeing was  $\sim 0''.6$  FWHM during this observation. Star positions derived via 2D Gaussian fitting were compared with targeted positions using the IRAF GEOMAP and GEOXYTRAN tasks. Because the pixel scale of the guiding CCD was not precisely known, the scale was one of the variables used in this fitting.

Figure 21 shows the deviations of the measured positions from the targeted ones. No systematic distortion is observed in the reconstructed image. The deviations are less than  $0''.1$  (figure 22). Although the pixel scale of the guiding CCD is not precisely known, the slice width and length derived in this method are shown in table 4 as a reference.

## 6.4 Throughput

The IFU throughput was estimated by dividing the object spectra by the sky spectrum, because the sky spectrum did not pass through the IFU optics. For this purpose, a blank sky was observed at six telescope positions using the 300R grism and the SO58 filters on 2018 March 2. Three flames with a 120 s exposure were obtained at each position. The obtained data were reduced using the FOCAS IFU reduction software, but flat-fielding was not applied. The resultant data cubes were integrated from  $6000 \text{ \AA}$  to  $9000 \text{ \AA}$  to increase the signal-to-noise ratio. The sky spectrum was extracted from one spaxel with the narrowest slit width because the width is the most coincident with the slice width of the slicer.

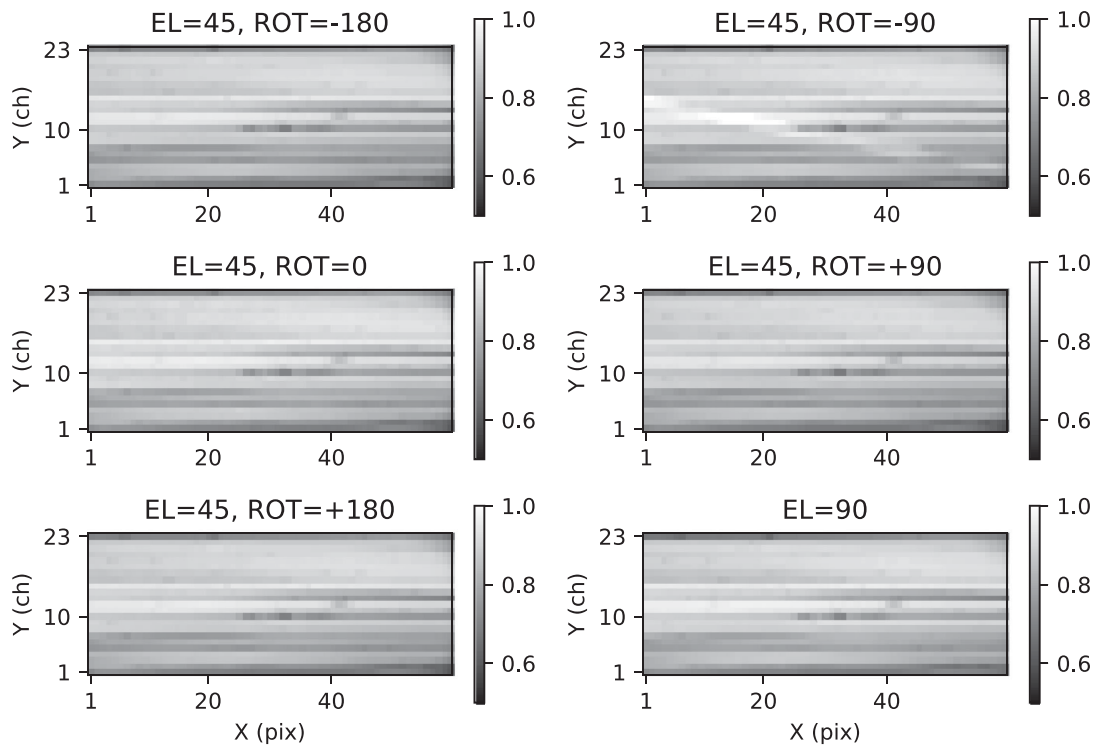
The IFU throughput does not significantly vary for the different telescope positions (figure 23). At an elevation (EL) of  $45^{\circ}$  and an instrument rotation angle (ROT) of  $-90^{\circ}$ , a linear pattern from the middle of the left to the bottom-right corner was observed. This is considered a star trajectory because a sidereal drive of the telescope was not used. Ch10 has lower throughput points around the center, which originated from chips at the slice mirror edge. Vignetting at the top- and bottom-right corners occurred in the magnification optics. Ch23 shows a lower throughput on the whole because of a large assembling error of the slice mirror.

Figure 24 shows the area fraction of the throughput derived from an averaged throughput image not including the image for  $\text{EL} = 45^{\circ}$  and  $\text{ROT} = -90^{\circ}$ . Because of a highly reflective dielectric coating, the mean and median throughputs are 85.0% and 87.3%, respectively. These values exceeded our targeted specification of  $>80\%$ . The lowest value is 61.9% at the bottom-right corner.

To measure end-to-end efficiencies, the spectrophotometric standard star, HD 37725, was observed on 2019 May 15 (figure 25). The data obtained are summarized in table 5. The number of flames was one for each disperser. The star was located at the center of the IFU FoV. The efficiencies are consistent with the expected values from the IFU throughput of  $\sim 85\%$  and the FOCAS efficiencies. These efficiencies are  $\sim 3$  times higher at  $6500 \text{ \AA}$  than those of Kyoto 3DII, and  $\sim 7$  times higher at  $9000 \text{ \AA}$  (Matsubayashi et al. 2016). Considering the difference in the spatial samplings ( $0''.435$  for FOCAS IFU and  $0''.096$  for Kyoto 3DII), the sensitivity of FOCAS IFU for extended sources is greatly improved from Kyoto 3DII.

## 6.5 Flat-fielding accuracy

To measure the flat-fielding accuracy, we used the same blank sky data as those used for the throughput estimation. In this case, the reduction procedure was normal, including flat-fielding using dome flat data. Data cubes were



**Fig. 23.** IFU throughput image at each telescope direction. The horizontal axis is the slice-length direction in units of binned pixels ( $0''.215/\text{pixel}$ ). The vertical axis shows the slice channel number. The linear pattern from the middle of the left to the bottom-right corner in the top-right panel is a star trajectory. EL and ROT denote the elevation and instrument rotation angle, respectively.

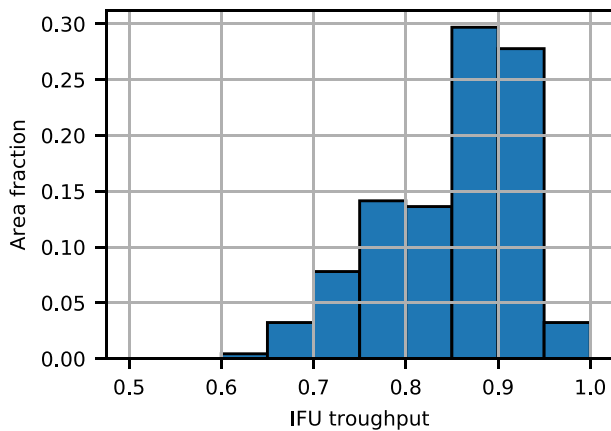


**Fig. 24.** Area fraction histogram of the IFU throughput. The vertical axis shows the area fraction with respect to the entire field of view.

integrated from 6000 to 9000 Å and normalized by the average of each image. The resultant images show the flat-fielding error (figure 26).

These images show significant variation depending on the telescope positions. As explained in subsection 6.4, the IFU shows vignetting because of misalignment, and the vignetting varies depending on the telescope position. In contrast, the dome flat was taken at a fixed position ( $EL = 90^\circ$ ). This causes the flat-fielding error. The largest error is at the bottom-right corner of  $EL = 90^\circ$  (9.0%). The

**Table 5.** Data obtained for the efficiency measurements.\*

Disperser	Filter	Exposure time (s)	Seeing (FWHM)
300R	SO58	10	$0''.6$
300B	None	5	$0''.6$
VPH650	SY47	30	$0''.7$
VPH520	None	20	$1''.1$

\*One exposure was taken for each disperser.

top-right corner and Ch23 of  $EL = 90^\circ$  also show larger errors (5.3% and 7.5%, respectively). These are unexpected results because the telescope positions are the same for the sky and the dome flat. This means that the light paths are slightly different between the sky and the dome flat. Except for  $EL = 90^\circ$ , the flat-fielding accuracy is within  $\pm 3\%$ .

## 6.6 Sky subtraction

Figure 27 shows the sky subtraction example. This example is the averaged spectrum over five blank sky regions in the NGC 4147 data (boxes in figure 20). The continuum residual is less than 2%. This residual can be fully explained by the flat-fielding uncertainty described in subsection 6.5, because the observations were conducted at  $EL \sim 47^\circ$  and  $ROT \sim -168^\circ$ . There are significant narrow residuals at

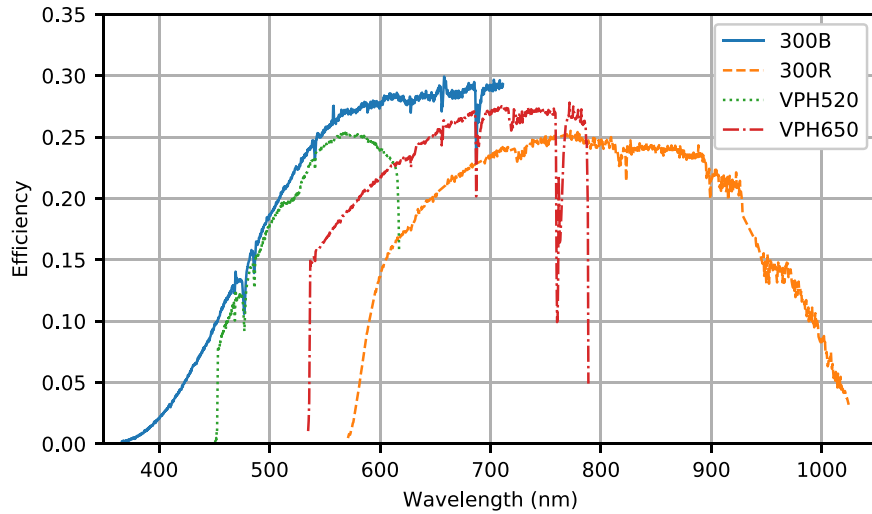


Fig. 25. Measured system efficiency including the atmosphere, telescope, FOCAS, and IFU. (Color online)

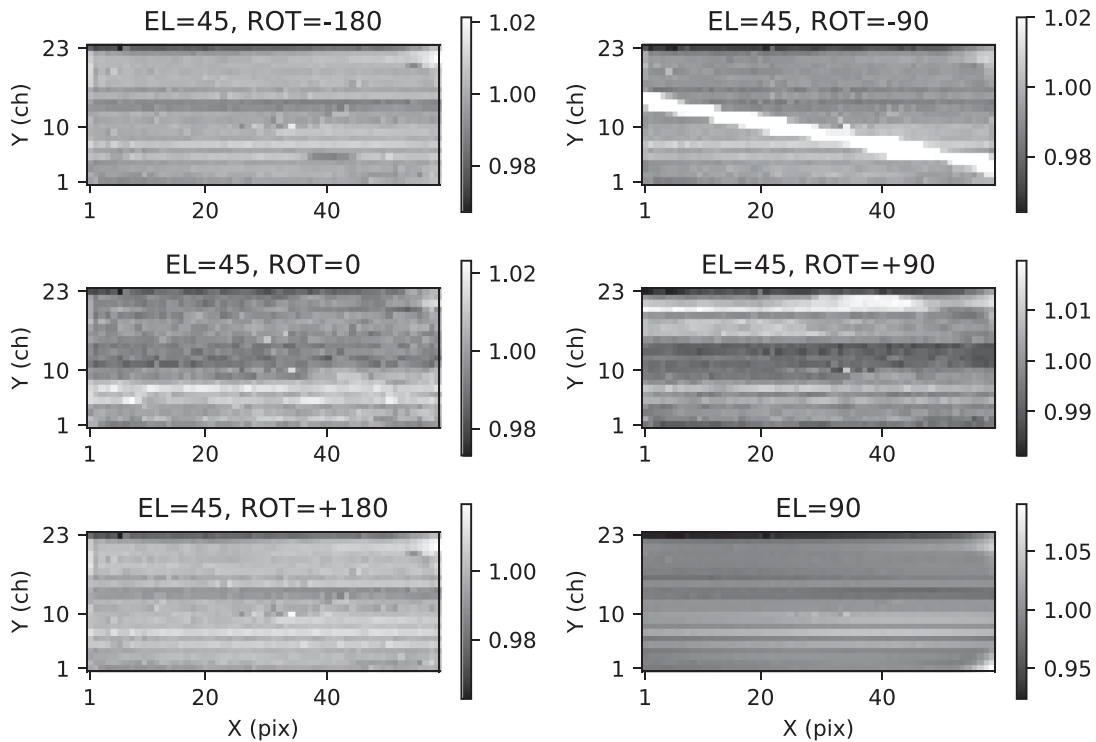


Fig. 26. Flat-fielding error for each telescope direction. The horizontal axis is the slice-length direction in units of binned pixels ( $0''.215/\text{pixel}$ ). The vertical axis shows the slice channel number. The linear pattern from the middle of the left to the bottom-right corner in the top-right panel is a star trajectory. EL and ROT denote the elevation and instrument rotation angle, respectively.

bright sky emission lines. These residuals would be caused by wavelength calibration uncertainty and point-spread-function variation across the field.

### 6.7 Absorption due to IFU optics

The IFU data show an absorption feature at  $\sim 4750 \text{ \AA}$  with an FWHM of  $\sim 10 \text{ \AA}$  and a depth of 30% (figure 28).

Because this feature does not exist in the sky spectrum, it originates from the IFU optics. The central wavelength of the feature varies with the channels and the field positions (figure 29). We thus conclude that the absorption arises from the multilayer dielectric coating on the slice mirrors or the pupil mirrors. Notably, the reflectivity measurement data provided from the company did not show such a deep absorption.



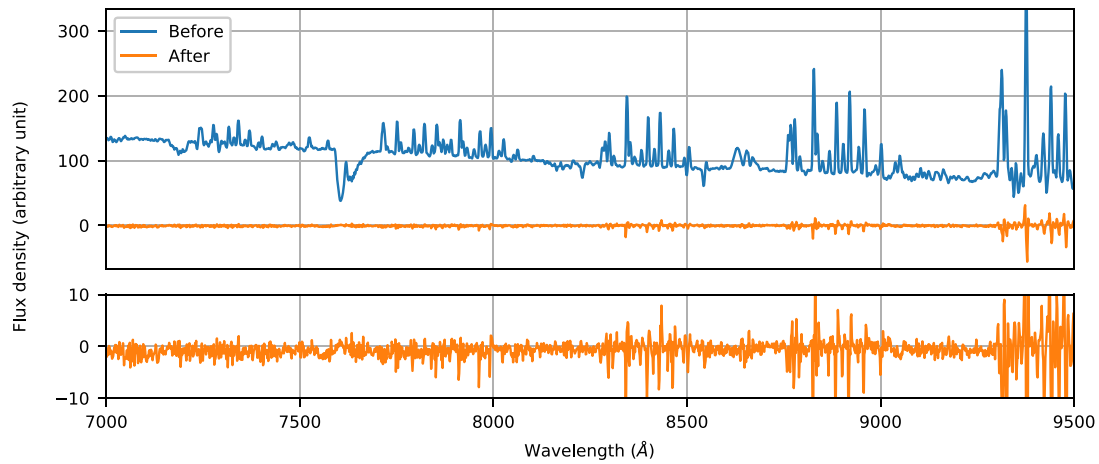


**Fig. 27.** Top: Averaged spectra of blank sky regions in the NGC 4147 data (figure 20) before and after the sky subtraction. Bottom: Magnified view of the sky-subtracted spectrum. (Color online)

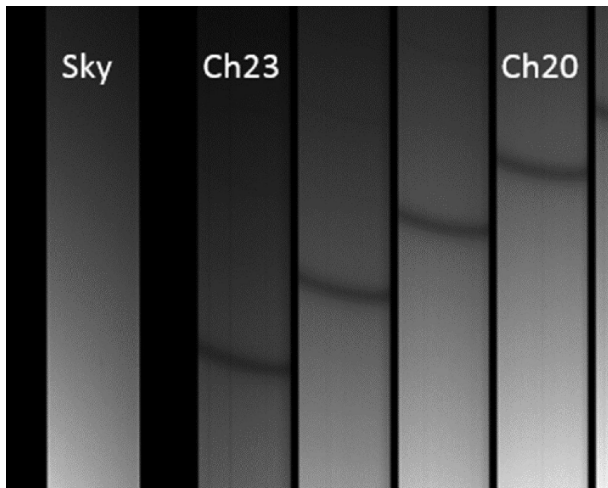


**Fig. 28.** Absorption features caused by the IFU optics. The absorption observed in Ch20–Ch23 does not exist in the sky spectrum.

## 7 Summary

We have described the optical design, mechanical structure, reduction software, and performance verification results of FOCAS IFU. The IFU is an image slicer system, which most efficiently utilizes the detector area among the three IFS methods. Using off-axis ellipsoidal surfaces for the pupil mirrors in the outer channels, the optical design successfully achieves a spot RMS diameter of less than  $0''.275$  for the entire wavelength range and over the field of view.

The major results of the performance verification tests are as follows:

- There is no significant degradation for a targeted spatial resolution of  $\sim 0''.43$ .
- The slice width and length are consistent with the design.

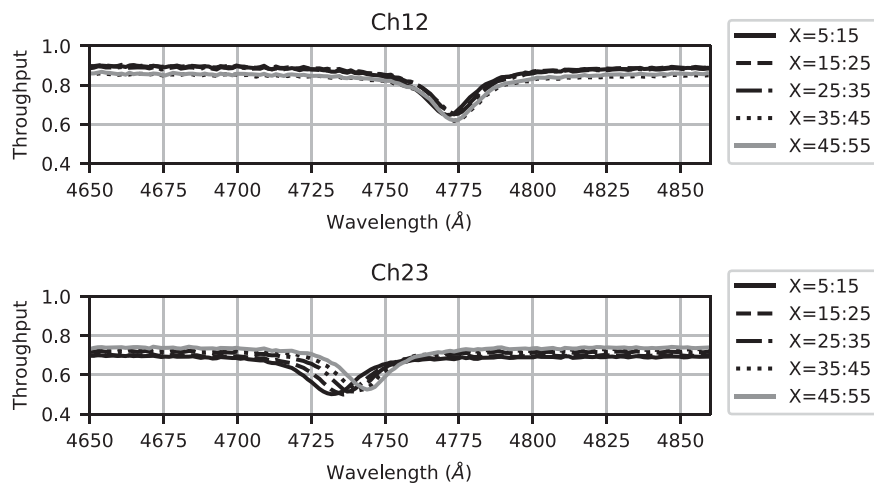


**Fig. 29.** Absorption profile variation in Ch12 (top) and Ch23 (bottom). The line style shows the place in the pseudo slit. For example, X=5:15 means that the spectrum is integrated from 5 pixels to 15 pixels along the pseudo slit.

- (c) Using the reduction software, the image reconstruction accuracy is less than  $0''.1$ .
- (d) The mean throughput of the IFU over the entire field is 85%. However, some field positions show lower throughputs because of vignetting caused by misalignment.
- (e) The vignetting variation causes flat-fielding uncertainty. Except for  $EL = 90^\circ$ , the uncertainty is within  $\pm 3\%$ . The largest uncertainty is 9% at the bottom-right corner of the  $EL = 90^\circ$  data.
- (f) An unexpected absorption feature is found around  $\sim 4750 \text{ \AA}$  in the IFU spectrum. This feature originates from the dielectric multilayer coating in the IFU.

The highly reflective dielectric multilayer coating is essential for achieving a high throughput. By developing FOCAS IFU, we identified technical challenges such as substrate deformation caused by its large stress, edge treatment for slice mirrors, and a measurement strategy to avoid unexpected absorption features. Because of these challenges, no vendor provides an image slicer with the coating. However, these issues must be addressed in future research to explore the deep universe.

## Acknowledgment

We thank the staff at the Advanced Technology Center, National Astronomical Observatory of Japan (NAOJ) for their help with development. We also thank SIGMAKOKI Co., Ltd. and Showa Optronics Co., Ltd. for their intensive efforts for manufacturing the IFU optics. We are grateful to Y. Matsuda, T. Saito, and T. Kawaguchi for valuable discussions about science cases, and also to K. Kushibiki for giving us the idea for figure 5. This IFU development was supported by JSPS KAKENHI Grant Number JP26400236 and the TMT-J Project Office, NAOJ, through its funding program

for research and development of TMT science instruments. This research has made use of “Aladin sky atlas” developed at CDS, Strasbourg Observatory, France.

## References

- Allington-Smith, J., et al. 2002, *PASP*, 114, 892
- Allington-Smith, J. R., Content, R., Dubbeldam, C. M., Robertson, D. J., & Preuss, W. 2006, *MNRAS*, 371, 380
- Astropy Collaboration, 2013, *A&A*, 558, A33
- Astropy Collaboration, 2018, *AJ*, 156, 123
- Bacon, R., et al. 2010, *Proc. SPIE*, 7735, 773508
- Content, R. 1997, *Proc. SPIE*, 2871, 1295
- Fernique, P., et al. 2015, *A&A*, 578, A114
- Gaia Collaboration, 2016, *A&A*, 595, A1
- Kashikawa, N., et al. 2000, *Proc. SPIE*, 4008, 104
- Kashikawa, N., et al. 2002, *PASJ*, 54, 819
- Kawaguchi, T., et al. 2018, *PASJ*, 70, 93
- Larkin, J. E., et al. 2003, *Proc. SPIE*, 4841, 1600
- McGregor, P., et al. 2003, *Proc. SPIE*, 4841, 1581
- Matsubayashi, K., Sugai, H., Shimono, A., Akita, A., Hattori, T., Hayano, Y., Minowa, Y., & Takeyama, N. 2016, *PASP*, 128, 095003
- Morrissey, P., et al. 2018, *ApJ*, 864, 93
- Ozaki, S., et al. 2012, *Proc. SPIE*, 8450, 84501L
- Ozaki, S., et al. 2014, *Proc. SPIE*, 9151, 915149
- Prieto, E., Le Fèvre, O., Saisse, M., Voet, C., & Bonneville, C. 2000, *Proc. SPIE*, 4008, 510
- Science Software Branch at STScI 2012, *Astrophysics Source Code Library*, ascl:1207.011
- Sharples, R., et al. 2014, *Proc. SPIE*, 9147, 91470W
- Smith, R. J., Collier, W. P., Ozaki, S., & Lucey, J. R. 2020, *MNRAS*, 493, L33
- Sugai, H., et al. 2010, *PASP*, 122, 103
- Tody, D. 1986, *Proc. SPIE*, 627, 733
- Tody, D. 1993, *ASP Conf. Ser.*, 52, 173
- van Dokkum, P. G. 2001, *PASP*, 113, 1420